frontiers | Frontiers in Physics

TYPE Original Research
PUBLISHED 09 January 2023
DOI 10.3389/fphy.2022.964696

OPEN ACCESS

EDITED BY
Mark Paris,
Los Alamos National Laboratory (DOE), United States

REVIEWED BY
Arnaud Le Fèvre,
Helmholtz Association of German Research Centres (HZ), Germany
Dario Lattuada,
Kore University of Enna, Italy

*CORRESPONDENCE
O. Z. Labun,
ozlabun@utexas.edu

SPECIALTY SECTION
This article was submitted to Nuclear Physics, a section of the journal Frontiers in Physics

RECEIVED 08 June 2022
ACCEPTED 15 December 2022
PUBLISHED 09 January 2023

CITATION
Jiao X, Curry CB, Gauthier M, Chou H-GJ, Fiuza F, Kim JB, Phan DD, McCary E, Galtier EC, Dyer GM, Ofori-Okai BK, Labun L, Labun OZ, Schoenwaelder C, Roycroft R, Tiwari G, Glenn GD, Treffert F, Glenzer SH and Hegelich BM (2023), High deuteron and neutron yields from the interaction of a petawatt laser with a cryogenic deuterium jet.
Front. Phys. 10:964696.
doi: 10.3389/fphy.2022.964696

High deuteron and neutron yields from the interaction of a petawatt laser with a cryogenic deuterium jet

X. Jiao[1], C. B. Curry[2,3], M. Gauthier[2], H.-G. J. Chou[2,4], F. Fiuza[2], J. B. Kim[2], D. D. Phan[1], E. McCary[1], E. C. Galtier[2], G. M. Dyer[2], B. K. Ofori-Okai[2], L. Labun[1], O. Z. Labun[1]*, C. Schoenwaelder[2,5], R. Roycroft[1], G. Tiwari[1], G. D. Glenn[2,6], F. Treffert[2,7], S. H. Glenzer[2] and B. M. Hegelich[1,8]

[1]Center for High Energy Density Science, University of Texas at Austin, Austin, TX, United States, [2]SLAC National Accelerator Laboratory, Menlo Park, CA, United States, [3]Department of Electrical and Computer Engineering, University of Alberta, Edmonton, AB, Canada, [4]Physics Department, Stanford University, Stanford, CA, United States, [5]Friedrich-Alexander-Universität Erlangen-Nürnberg, Erlangen Centre for Astroparticle Physics, Erlangen, Germany, [6]Applied Physics Department, Stanford University, Stanford, CA, United States, [7]Institute for Nuclear Physics, Technical University Darmstadt, Darmstadt, Germany, [8]CoReLS, Institute for Basic Science (IBS), Gwangju, South Korea

A compact high-flux, short-pulse neutron source would have applications from nuclear astrophysics to cancer therapy. Laser-driven neutron sources can achieve fluxes much higher than spallation and reactor neutron sources by reducing the volume and time in which the neutron-producing reactions occur by orders of magnitude. We report progress towards an efficient laser-driven neutron source in experiments with a cryogenic deuterium jet on the Texas Petawatt laser. Neutrons were produced both by laser-accelerated multi-MeV deuterons colliding with Be and mixed metallic catchers and by d $(d,n)^3$He fusion reactions within the jet. We observed deuteron yields of 10^{13}/shot in quasi-Maxwellian distributions carrying ~ 8 – 10% of the input laser energy. We obtained neutron yields greater than 10^{10}/shot and found indications of a deuteron-deuteron fusion neutron source with high peak flux ($>10^{22}$ cm^{-2} s^{-1}). The estimated fusion neutron yield in our experiment is one order of magnitude higher than any previous laser-induced dd fusion reaction. Though many technical challenges will have to be overcome to convert this proof-of-principle experiment into a consistent ultra-high flux neutron source, the neutron fluxes achieved here suggest laser-driven neutron sources can support laboratory study of the rapid neutron-capture process, which is otherwise thought to occur only in astrophysical sites such as core-collapse supernova, and binary neutron star mergers.

KEYWORDS

laser-driven neutron source, high-flux neutron source, rapid neutron capture process, laboratory astro-nuclear physics experiment, laser-driven fusion, laser-driven ion source

1 Introduction

The synthesis of approximately half of the atomic nuclei heavier than iron is theorized to occur *via* the rapid neutron-capture process (r-process) in astrophysical environments of extreme temperature and density. While such temperature and density are unlikely to be recreated in the lab, a broadly-recognized goal is to develop experiments to study the nuclear scattering and excitation dynamics of multi-neutron capture, which is estimated to require neutron fluxes greater than 10^{22} cm^{-2} s^{-1} [1]. Beyond nuclear astrophysics, fast neutrons produced in a compact, ultra-short pulse source, would have wide ranging applications including high energy density physics [2], materials science [3], and medical research [4]. For this reason, high-flux neutron sources remain an important subject of research and development. Laser-driven neutron sources in particular are a promising approach [5], having already achieved much higher peak neutron fluxes than fission reactors (~ 10^{15}/cm^2/s) or spallation (~ 10^{17}/cm^2/s) sources in laboratory experiments, potentially in a more compact facility [6].

The highest neutron yields achieved by laser-driven sources are from inertial confinement fusion (ICF) [7] experiments. The most successful shots at the National Ignition Facility (NIF) produced $>10^{15}$ neutrons in less than a nanosecond [8] suggesting that neutron fluxes greater than 10^{24}/cm^2/s are achieved just outside the cm-long hohlraum. However, ICF user facilities like OMEGA [9] or the NIF [10] are too large to be available for smaller-scale nuclear physics studies with neutrons for the foreseeable future.

The advent of ultrahigh intensity lasers thanks to chirped pulse amplification [11] has enabled the production of neutrons in a much more compact arrangement [3, 12–24]. Several schemes have been tested on laser systems ranging in scale from millijoules [22] to kilojoules [3]. Among them, the most promising method is the ion-driven neutron source approach [20] because of its comparatively high efficiency and neutron yield. Experiments have demonstrated a directional peak yield of up to 1×10^{10} n/sr/shot [19]. The scheme is usually employed in "pitcher-catcher" configuration, where the laser interacts with a thin (~μm) pitcher target to accelerate ions, typically protons or preferably deuterons. These ions then interact with a cm-scale, low-Z "catcher" target, beryllium-9 [18], lithium-7 [25] or deuterated plastic [23], undergoing nuclear reactions and producing neutrons in the process. Using break-out afterburner acceleration in the relativistic transparency regime [19], this method could achieve an overall laser-to-neutron energy conversion efficiency of ~ 6×10^8 n/J compared to ~ 4×10^8 n/J for TNSA acceleration driven laser-neutron generation, ~ 4×10^6 n/J for laser-electron driven neutron source [24], and only ~ 10^5 n/J for laser-cluster fusion neutron source [17].

We report on a novel approach to laser-driven neutron generation. For the first time in a petawatt laser facility, cryogenic deuterium jet targets were used to efficiently generate neutrons. These targets offer several advantages over the deuterated plastic foils used in previous experiments [16, 18, 19, 26], including near-critical electron density allowing access to the relativistic transparency regime and potential for high repetition rate target preparation [27]. The thin, above critical density target results in efficient ion acceleration (~ 10% of laser energy transferred to ions), and the higher yield (~ 10^{13}/shot) and energy deuteron beam produces a higher yield of neutrons in the pitcher-catcher configuration. We find higher neutron yields detected in the bubble detectors than can be explained by deuteron-converter interactions. E other sources and simulating the laser-plasma interaction, we consider the most plausible explanation is that, in addition to being efficiently accelerated out of the target, deuterons in the target are volumetrically heated and produce a significant number of neutrons by the d $(d,n)^3$He reaction. The deduced fusion neutron yield is consistent with simulation estimates and, considering the small source size ($\lesssim$ 100 μm), suggests a route to the ultra-high fluxes required for r-process studies.

2 Experimental setup

The experiment was carried out at the Texas Petawatt laser [28] facility at the University of Texas at Austin. The experimental setup is depicted in Figure 1. The 1057 nm Nd:Glass laser delivered 90–140 J, 140 fs laser pulses to irradiate the deuterium jet targets. Using an *f*/3 off-axis parabolic mirror, the laser beam was focused to a spot size of 6 μm full-width half-maximum (FWHM) to an average encircled laser intensity of $>10^{21}$ W/cm^2. A plasma mirror was installed 5 cm before the target to remove pre-pulses and steepen the rising edge of the main pulse (see temporal profile in Appendix A), reaching a contrast ratio of $>10^5$ at 10 ps before the arrival of the main beam. The plasma mirror reflectivity was estimated to be approximately 80%.

The deuterium jet was made by a cryogenic microjet system developed at SLAC [29, 30]. Deuterium gas is liquified and held at 19–21K in a copper source assembly cooled by a continuous-flow helium cryostat. The liquid deuterium enters the chamber through a 2×40 μm rectangular aperture and rapidly solidifies a few 100 μm from the nozzle by evaporative cooling. The resulting cryogenic deuterium jet is a relatively flat planar sheet of width 15 μm between two 5 μm diameter cylindrical columns, as illustrated in Figure 1A, running at a speed of 50–100 m/s into vacuum [31]. At this temperature, the density of the deuterium is expected to be $n_d \simeq 6 \times 10^{22}$ cm^{-3}. The jet-laser overlap was monitored and adjusted using two orthogonal probe imaging systems.

Either a radiochromic film (RCF) stack or a Be converter was placed downstream of the laser forward direction. The RCF stack consisted of alternating layers of aluminum foil, copper sheets and calibrated RCF films [32] of different thicknesses to measure

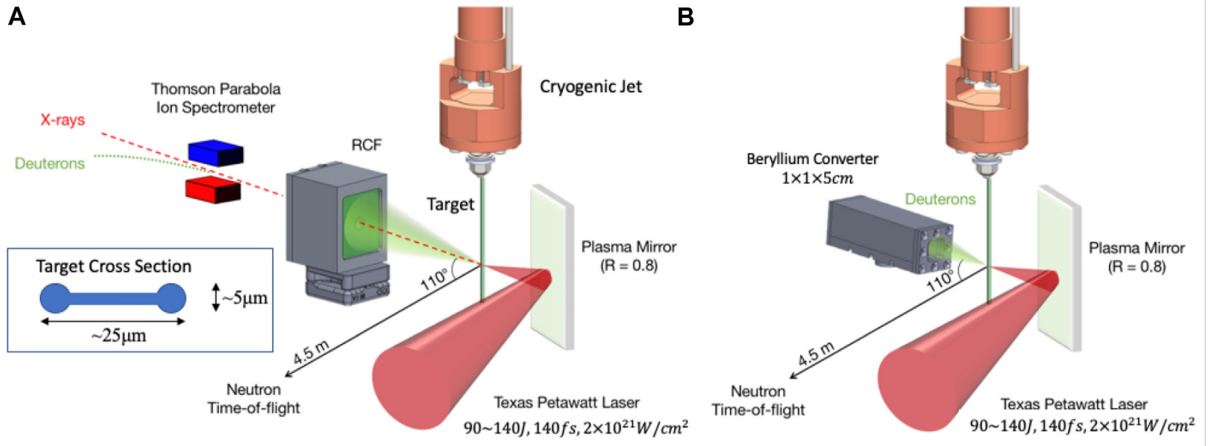

FIGURE 1
(A) Experiment setup with RCF stack. Inset: cross section of the deuterium ice targets. **(B)** Experiment setup with beryllium converter.

the deuteron beam divergence profile and rough spectrum. The precise composition of the stack is given in Appendix B. The 2.7 × 2.3 cm^2 RCF stack was centered on the laser axis 4.5 cm behind the target. It had a centered 5 mm diameter hole providing line of sight for a Thomson parabola spectrometer (TPS). The TPS was analyzed in conjunction with the RCF stack to provide an absolutely calibrated, high resolution measurement of the deuteron beam energy spectrum. A second TPS and an electron spectrometer were respectively located 30° and 36° counter clockwise from the laser axis. The high voltage setting on the TPS was not turned on during the measurements since the irradiated target introduces a significant load on the vacuum system resulting in pressures which cause electrical arcing in the TPS thereby corrupting the signal recorded on the imaging plate. However, a previous experiment which utilized differential pumping to separate the TPS from the vacuum chamber, demonstrated that other ion species are negligible compared to the main source because of the high purity of the deuterium gas (D_2, 99.6% + HD, 0.4%) used to create the cryogenic deuterium jet target [33].

In addition to measuring the energy-resolved spatial distribution of the deuteron beam, the RCF stack also acts as a neutron converter where laser-accelerated deuterons produce neutrons *via* breakup reactions. We also investigated enhancing neutron production by installing a 1 × 1 × 5 cm^3 Be converter centered on the laser axis at a distance of 2.7 cm. Due to its light atomic weight and high (d,n) reaction cross section, the Be converter is expected to produce a higher neutron yield than the RCF stack. The beryllium converter was housed in an aluminum casing with a 100 μm thick aluminum window on the side facing the laser-plasma interaction. This shields the beryllium from the transmitted laser pulse, while still allowing the majority of MeV-energy deuterons to pass through.

A neutron time of flight (n-TOF) detector was used to measure the neutron energy spectrum 4.5 m away from the target chamber center (TCC) and 110° away from the laser propagation direction, which was the only available line-of-sight given the radiation shielding. The n-TOF consists of a fast plastic scintillator (EJ-200), a photomultiplier (XP2020) and a fast-digital oscilloscope (TDS5104). The strong x-ray signal from the laser target interaction was shielded by a 32.5 mm thick Cu plate to reduce the decay signal width (FWHM) to below 25 ns. The thickness is chosen to ensure the neutron signal remains greater than the x-ray-generated background, which thereby served as a time reference for the neutron energy analysis. The response function of the scintillator was measured beforehand and the width (FWHM) was found to be around 10 ns per volt. For our setup, this would introduce a 10% uncertainty in the energy measurement and it affects the low energy range less than the high energy range. Ten bubble detectors [34] were positioned in the laser plane at various angles around the target chamber (−177° – 90° from target normal, to measure the fast neutron flux at the detector position. The bubble detectors' sensitivities varied between 2–2.5 bubbles/mrem. Distances of the bubble detectors were measured using the front of the Be converter or the front of the RCF stack as a reference point as our analysis, presented in the following sections, suggests this is the primary source of neutrons.

3 Results

A typical deuteron energy spectrum measured at 0 and 30° from the laser forward direction, as well as the reconstructed average spectrum from the dose recorded on each RCF film are

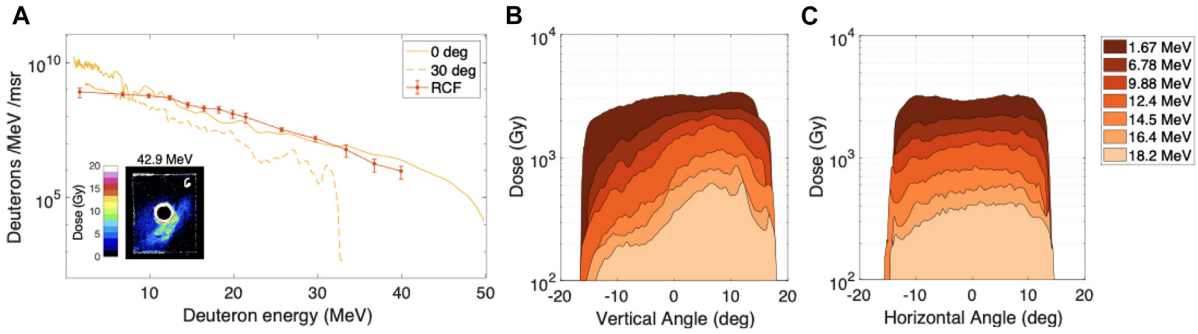

FIGURE 2
Deuteron beam characteristics for shot 11,557: **(A)** Deuteron spectrum, measured in the laser forward direction through a 5 mm diameter hole in RCF stack centered on the laser plasma acceleration with a TPS. Inset: Deuteron spatial profile on last RCF film which corresponds to 42.9 MeV **(B, C)** Average deuteron emission distribution in the vertical and horizontal direction from the first 7 HD-V2 layers of the RCF stack.

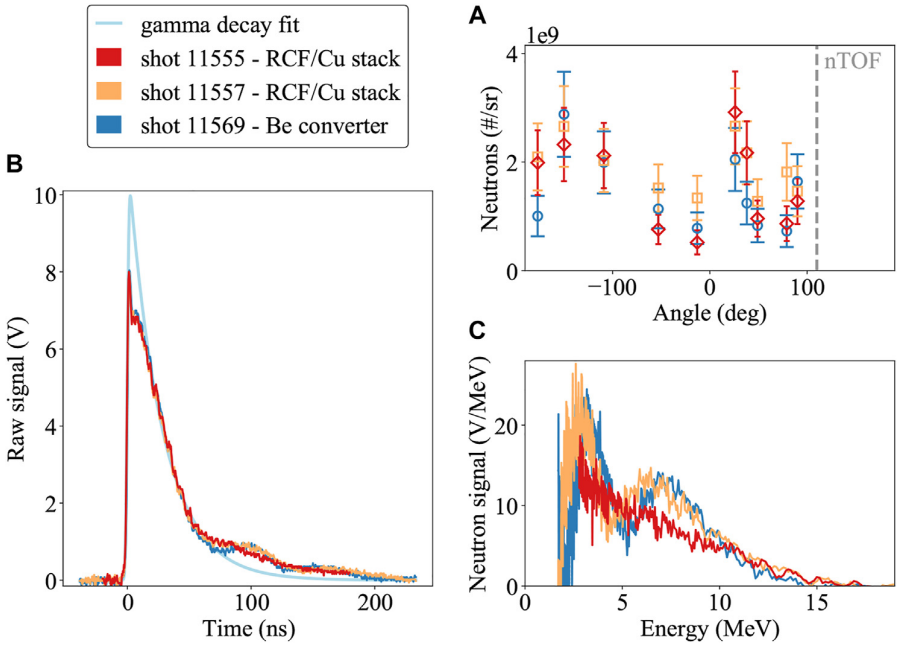

FIGURE 3
(A) Number of neutrons detected in each bubble detector, as a function of their angles with respect to the laser-forward direction. Fluxes are given assuming a source at the front surface of converter or RCF stack. Total neutron yield is 2.0×10^{10} assuming an isotropic source in 4π. **(B)** The neutron TOF signals with gamma decay fit for shot 11,557 (light blue) overlaid. **(C)** The neutron spectrum in V/MeV as a function of detected neutron energy after the gamma background is subtracted.

shown in Figure 2A. Note that the absolute flux was calculated using the energy-dependent image plate calibration from [35] in conjunction with doses extracted from the RCF films in the laser forward direction. The deuteron spectrum follows a semi-Maxwellian distribution, indicative of a TNSA-dominated regime [31], with a cut-off energy of 50 MeV (shot 11,557) at 0 deg. Consistent with a previous study using planar cryogenic hydrogen jets [31], the deuteron beam is comprised of two main components which are attributed to the planar central region and cylindrical rims of the cryogenic jet. The former produces a

conical beam with a half-angle decreasing from approximately 20° at the lowest energies to less than 10° near the cut-off energy (Figure 2B). The latter produces a near azimuthally symmetric deuteron emission with similar confinement along the jet axis as illustrated in Figure 2C.

The neutron yield was measured using the bubble detector array and the neutron spectrum measured using the n-TOF detector for 3 consecutive shots. For shots 11,555 and 11,557, deuterons were impinging on the RCF stack as shown in Figure 1A, while for shot 11,569, the Be converter was implemented in the setup replacing the RCF, see (b).

Absolute neutron numbers at the location of the bubble detectors were calculated by converting bubble counts to dose in mrem using the manufacturer provided sensitivity of the individual detectors. Dosages (mrem) were then converted to neutron flux (n/sr) using the conversion relation provided in [18] and the distances of the detectors to the RCF or converter. Figure 3A shows the calculated neutron flux as a function of angle with respect to laser forward direction for the three recorded shots. The error bars shown in the plot are a combination of the statistical error of the measurement ($\sqrt{N}/N$) and the response fluctuation of the bubble detector across its sensitivity range. This response dependent error (19%) is determined by calculating the standard deviation of the response measurement conducted by [18] across an energy ranging from 0.3 to 32 MeV. Calculated fluxes across the three shots ranged from (5.2×10^8–2.9×10^9) n/sr. As seen in Figure 3A the neutron fluence distribution is predominantly isotropic with two broadened peaks visible at −150 and 30°. Monte Carlo simulations described in the next section show that the peak at 30° is due to the forward-directed conical-beam component of the deuteron distribution described above. Averaging over the detected neutron flux for all shots and integrating over 4π, in the same way as previously published works, we obtain a total neutron yield of $\sim 2 \times 10^{10}$ n/shot. Note that due to the lack of neutron flux measurements outside of the laser propagation plane, this number can be viewed as the ideal case and as an upper bound to the actual on-shot neutron yield. Future measurements will give more insight into the neutron flux distribution outside the laser plane. Even though the flux we calculate is based on the important assumption of isotropy in 4π, the estimate still agrees within error bars with Monte Carlo simulation described below.

Figure 3B shows the raw neutron traces acquired by the n-TOF detector for all three shots (11,555, 11,557 and 11,569). The spectra were extracted first by subtracting the signals corresponding to the x-rays from the overall time of flight signals, which is accomplished by fitting the X-ray peak with a skewed Gaussian model

$$f(x) = A\, e^{\alpha\left(\mu - x + \frac{\alpha\sigma^2}{2}\right)}\left[1 - \mathrm{erf}\left(\frac{\mu - x + \alpha\sigma^2}{\sqrt{2}\,\sigma}\right)\right] \quad (1)$$

with the center of the peak μ, the standard deviation σ, the amplitude A, the fit factor α and the error function erf. As an example the gamma peak decay fit for shot 11,557 is displayed in Figure 3B as the light blue curve. We fit the decay line after the first 16 ns to avoid the interference of the fast decay process, corresponding to the very sharp peaks at time zero. Then the neutron signal was converted from the time domain to energy domain ($\mathrm{d}V/\mathrm{d}t \rightarrow \mathrm{d}V/\mathrm{d}E$) by setting a 10% threshold on the X-ray peak to determine the laser-target interaction time. Figure 3C shows the three different spectra as a function of energy in MeV and the neutron signal in terms of V/MeV. By allowing systematic uncertainties in the x-ray signal subtraction, we estimated the error on the neutron spectrum to be less than 10%.

In shot 11,555, the spectrum is monotonically decreasing with an endpoint energy $E_n \simeq 15$ MeV, consistent with simulations of deuteron break-up on Be, Al in the chamber walls and other experimental apparatus. In shots 11,557 and 11,569, we identify two distinct peaks, one around 2.7 MeV for 11,557 and 3.2 MeV for 11,569, the other broader and peaked around 6 MeV, suggesting two populations of neutrons with different origins.

4 Discussion

4.1 Neutron source modeling

The high yield of fast deuterons enables several channels for neutron production. Deuterons produce neutrons colliding with nuclei in the intended catcher or with experimental apparatus, mostly due to break-up of the deuteron. Deuterons can also fuse to produce neutrons *via* the $d\,(d,n)^3$He reaction. Deuteron break-up can occur anywhere in the target chamber, from the catcher near the center to the chamber walls near to the bubble detectors, whereas $d\,(d,n)^3$He reactions are only likely to occur within the deuterium plasma. These source distributions are very different but cannot be distinguished with the layout of detectors in the experiment, and we must therefore rely on Monte Carlo simulations to predict and interpret the neutron signal in each detector.

First, to estimate the yield from deuteron collisions with the Be converter, the RCF stack or other experimental apparatus, we constructed a simplified GEANT4 [36] model of the target chamber, including the aluminium walls and optical breadboard. The simulation includes seven bubble detectors placed at the angular positions −177°, − 150°, − 109°, − 53°, − 12°, 26°, 90°, with respect to the laser forward direction, and one TOF at 110°, mimicking the neutron diagnostics in the actual experimental setup. The deuteron source is modelled by the combination of two components as described earlier in the Results section: (1) a conical component with a 20° half-angle

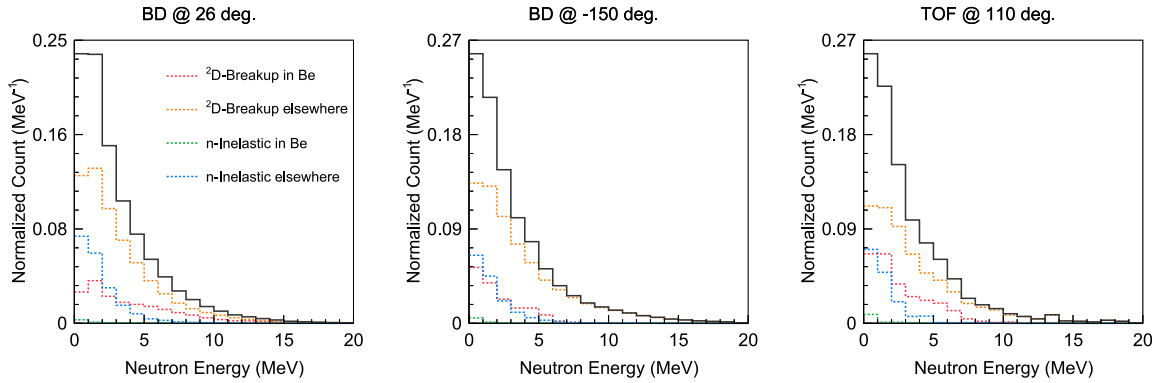

FIGURE 4
Non-fusion neutron spectrum from GEANT4 simulation obtained in the bubble detectors at 26°, −150° and the n-TOF at 110° with respect to the laser-forward direction are shown. The spectrum is broken down by the processes that created the neutrons: deuteron break-up on Be converter (red) or elsewhere in the chamber (orange), and neutron inelastic scattering in Be converter (green) or elsewhere (blue).

cone of emission guided by the measured spatial distribution on the RCF stack with the energy spectrum from the TPS at 0°; and (2) an azimuthally symmetric ring that extends ± 20° above and below the plane perpendicular to the jet axis with the deuteron energy spectrum measured by the TPS at 30°. The numbers of deuterons in each component are set equal, to stay consistent with the observation that the average flux seen by the TPS at 0° is about one order of magnitude larger than that at 30°. Due to the semi-Maxwellian energy distribution and accounting for changes in reaction cross-sections as a function of deuteron energy, neutrons are predominantly produced by the deuterons from the lower energy part of the spectrum (< 20 MeV). We may therefore neglect the variability in the beam divergence as a function of energy without loss of accuracy. The virtual detectors in the simulation retain information (type and event location) about the parent process that produced a detected neutron, along side with its kinematic variables (energy and momentum). This level of detail allows us to resolve different origins of non-fusion neutrons. To compare the GEANT4 Monte Carlo results with the experimental data, the simulation results are scaled to the actual deuteron numbers, which are measured in the Thomson parabola spectrometers and the RCF stack (if available for the shot).

GEANT4 contains a built-in model for nuclide break-up based on the Fermi model, which assumes the nuclide begins near mass shell. Consequently, this break-up model inevitably produces an exponential neutron spectrum, because it has no information about the threshold or cause of the nucleus' excitation. Varying the input parameters for the break-up model does not change this spectral shape as shown in Figure 4. For this reason, neutrons emitted from the RCF stack and the Be converter exhibit almost the same exponential decay spectral profile with energies up to 16 MeV. However, GEANT4's break-up model is generic and not tied to data; a back-of-the-envelope calculation suggests it overestimates the neutron yield considering the available cross section data for d-Be [37] and d-Al [38] collisions. Since these cross section data and models cover only a limited range of deuteron energies, we minimally extended the cross section data so that the thick target yields reproduced experimental data for a monoenergetic deuteron beam incident on Be [39] and Al targets [40, 41]. Uncertainty in these cross section data is primarily from the sparseness of data at higher deuteron energy $E_d \gtrsim 10$ MeV, and the resulting uncertainty in the neutron yields given the deuteron spectra in Figure 2 is less than 1%. The GEANT4 simulation results for the number of neutrons arriving at each bubble detector are corrected with these experimentally-validated cross sections. In addition to deuteron break-up as a primary source, neutrons can inelastically scatter in the same medium and produce additional, secondary neutrons. Neutron re-scattering contributes a non-negligible 10%–15% enhancement of the neutron yield shown in Figure 5.

The neutron numbers estimated from the bubble detectors data are compared against those predicted from the GEANT4 simulation in Table 1. Whether Be catcher or RCF stack was in place, deuteron scattering in the Al experimental apparatus contributes the largest share of neutrons in the bubble detectors. In shot 11,569 with Be, the apparatus is the source of roughly 3 times as many neutrons as the catcher. Given the relative number of deuterons striking the apparatus versus the catcher and the relative probability of neutron production in Al versus Be, we deduce that the geometric enhancement from the bubble detector being immediately adjacent to the chamber wall is roughly a factor of 3. This agrees with a simple analytic model of the geometric enhancement. For shots 11,555 and 11,557, the neutron production probability in the RCF stack is estimated two

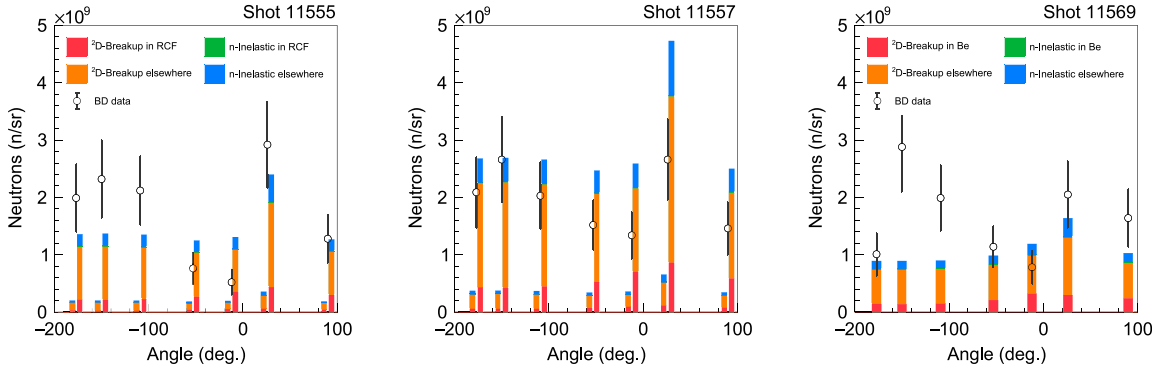

FIGURE 5
Comparison between the non-fusion neutron contribution from Geant4 simulation and the bubble detector measurements. Fluxes are given assuming a source at the front surface of converter, which coincides with the center of the target chamber to well-within the error.

TABLE 1 The measured neutron yield is determined by averaging the yields in the bubble detectors and assuming the same apparent flux holds isotropically. This procedure compares favorably with the GEANT4 simulation in the second row.

Neutron yield	Shot 11,555	Shot 11,557	Shot 11,569
Measured ($\times 10^{10}$)	2.14 ± 0.90	2.47 ± 0.97	2.06 ± 0.84
GEANT4 ($\times 10^{10}$)	0.28–1.85	0.51–3.65	1.35

ways: optimistically the neutron production probability is as high as Be and more pessimistically the neutron production probability is similar to Al, represented respectively by the taller and shorter colored bars in Figure 5. In reality, the RCF stack is layered construction of polymer and Cu; both materials have deuteron break-up cross sections greater than Al but less than Be [38]. Thus, the two estimates are upper and lower bounds on the neutron yield from the RCF stack. In shots 11,555 and 11,569, deuteron scattering in the catcher and apparatus is comparable in order of magnitude but systematically lower than the total measured neutron yield. In shot 11,557, the simulation results suggest that deuteron scattering in the apparatus suffices to explain the measured neutron yield.

The TOF spectra can provide further evidence to identify the likely origins for the neutrons. The GEANT4-predicted spectrum is consistent with the spectrum in shot 11,555, suggesting the majority of neutrons in that shot were derived from deuteron scattering in the apparatus. This evidence is consistent with the analysis of the bubble detector yields in Figure 5.

Interpreting the spectra in shots 11,557 and 11,569 is more difficult. A thermal d (d,n)^{3}He fusion spectrum fit [42] to the lower energy peak in 11,557 would suggest deuterons in the target achieved a Maxwellian distribution with $T \gtrsim 200$ keV. A similar fit is not consistent with the 11,569 spectrum due to the shift of the peak to 3.2 MeV. Moreover a fusion interpretation of the lower-energy peak in shots 11,557 and 11,569 is difficult to sustain in view of time, volume and energy constraints. Then to explain the second peak, we would need to identify an independent source of neutrons producing similar flux with a Gaussian spectrum centered near $\simeq$ 6 MeV.

While the two-peak structure of the spectra in shots 11,557 and 11,569 defies easy explanation, the endpoint of the spectrum in all 3 shots, $\simeq$ 15 MeV, agrees with the GEANT4 simulation. This suggests that the detector responded to a neutron pulse similar to that predicted, but the waveform may have been distorted. The same detector was subsequently used in other laser-plasma experiments without presenting a similar signal, and the waveform is not recognized as caused by known detector errors or miscalibration.

4.2 In-target fusion hypothesis

Figure 5 shows the bubble detector neutron counts and the background computed from available cross-section data and Monte Carlo simulation described above. On two out of the three shots, we find a small but significant difference between the predicted neutron yield from break-up and the measured neutron yield. Having accounted for the most significant sources of neutrons from non-fusion reactions, we identify the remainder with *dd* fusion (d (d,n)^{3}He) reactions in the target. Averaging the difference between the observed neutron number and the simulation and assuming isotropic emission from the plasma, we estimate that $\simeq 1.2 \times 10^9$ neutrons were produced by *dd* fusion. The most significant uncertainties in this estimate are due to incomplete information on the deuteron beam, which we

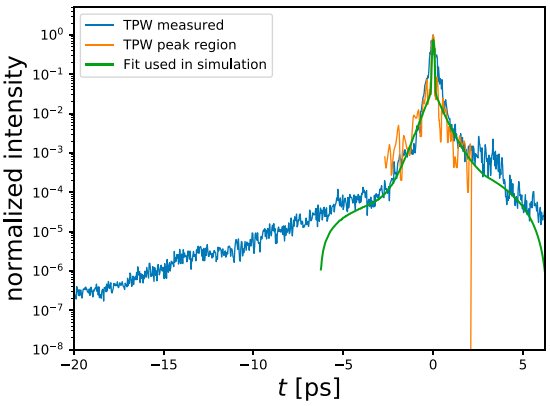

FIGURE 6
Temporal intensity profile of the Texas Petawatt laser pulse, without plasma mirror.

have modeled from the RCF and TP spectra and comparison with past experiments. In particular, the two-component model of the deuteron beam implies that ≳ 8% of the on-target laser energy is transferred to the deuterons. With shot-to-shot fluctuations in the laser energy and plasma mirror reflectivity accounted for, shot 11,557 showed the highest energy transfer ≳ 10%, shot 11,555 showed the lowest energy transfer, in the range 8%–9%, and shot 11,569 showed ~ 10%. In shot 11,569, a spectrum is only available from the 30-degree TP but the neutron yield suggests that the forward-directed component of accelerated deuterons was similar or higher than 11,555 and 11,557. Energy conversion ≥ 10% into ions has been achieved before, but required a complicated multi-pulse scheme [43], suggesting our model of the deuteron beam may err high in deuteron number compared to the experiment. It would follow that the GEANT4 simulations err high on the predicted neutron yield and the derived fusion neutron yield is low.

In order to investigate the deuteron heating associated with the intense laser-plasma interaction and the possibility of high neutron yield from *dd* fusion in our experimental setup, we have performed two-dimensional (2D) particle-in-cell (PIC) simulations with the OSIRIS code [44, 45]. We model the interaction of a laser with 88 J, peak $a_0 = 24$, 8.5 μm spot size, and pulse duration of 135 fs with a deuterium slab jet of density 48 n_c and thickness of 2 μm. We model the laser pre-pulse from 6 ps before the main pulse by fitting the temporal profile of the Texas Petawatt laser (see Figure 6) and including this pre-pulse profile in the simulation. In our simulations the laser (with frequency ω_0) is launched along the z direction from the left boundary. The electron-deuteron target plasma is simulated with 36 particles per cell per species, and the total simulation domain of ≃ 1400 μm × 700 μm is resolved with a spatial resolution (cell size) of 0.25 c/ω_0. The time step is chosen according to the Courant–Friedrichs–Lewy condition. Open (absorbing) boundary conditions for both particles and fields are used in both the longitudinal and transverse directions. We have tested different resolutions and numbers of particles per cell to ensure convergence of the results and have used a third order particle interpolation scheme for improved numerical accuracy.

We observe that the laser pre-pulse starts expanding the central region of the target before the main pulse arrives. The main pulse then interacts with the pre-expanded target, strongly heating the electrons, and accelerating the deuterons. The laser eventually breaks through the target *via* relativistic transparency, further accelerating the deuterons [46, 47]. Figure 7 summarizes the main results in terms of deuteron heating and neutron production from *dd* fusion reactions. The neutron reaction rates were obtained by integrating the *dd* fusion cross-sections [48] from the local deuteron distribution functions in the simulations. In panel (a) we see the spatial distribution of the *dd* neutron rate 6 ps after the arrival of the main pulse. While deuterons are significantly heated in the central region, the neutron yield there is moderate due to the lower plasma density. We find that most of the neutron generation occurs just outside this central region, in two hot spots, where the density is still comparable to the initial target density but deuterons have been heated to T_d ~ 10 keV (panel b). Moreover, we find that in this region, the deuteron distribution has significant non-thermal tails above 25 keV increasing the neutron production rate as seen in panel (b). We observe that most of the neutron generation occurs within the first 4 ps after the interaction of the main pulse. By assuming cylindrical symmetry around the laser axis we calculate a total neutron yield from *dd* fusion reactions of 4×10^9. However, it is important to note that in the actual 3D configuration of the experiment the target size should be limited in the transverse direction not captured by 2D simulations, which should decrease the total yield. While 3D PIC simulations will be needed to produce a more precise calculation of the total neutron yield, our simulation results indicate the possibility of producing order 10^9 *dd* fusion neutrons consistent with the experimental analysis discussed above.

With 10^9 neutrons produced over ~ 10 ps, the surface neutron flux on a 100 μm-radius sphere around the deuterium plasma is estimated ≃ 8×10^{22} n/cm^2/s, which is almost 10^6 times higher than the neutron flux from the ion-driven method [26] due to its smaller source size and shorter pulse duration. In the ion-driven method, the neutron pulse duration is determined by the flight time of ion passing through the reaction region, which is usually in ns level, as opposed to tens of ps over which the reaction rate is significant.

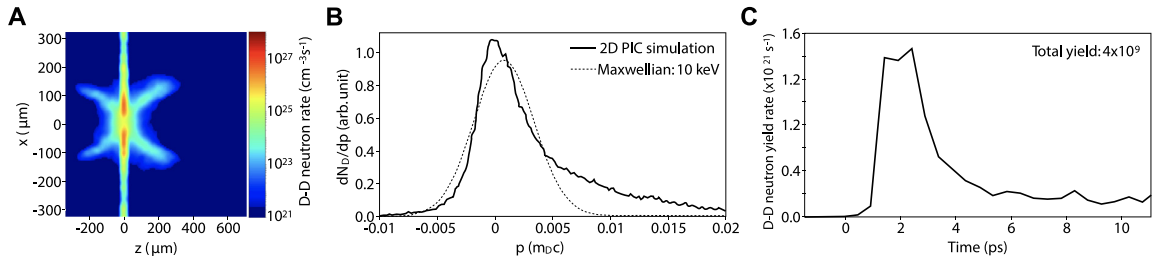

FIGURE 7
Neutron generation from *dd* fusion reactions obtained in a 2D PIC simulation of the interaction of the Texas Petawatt laser with a deuterium target. **(A)** *dd* fusion neutron rate 6 ps after the main pulse arrival. **(B)** Local deuteron momentum distribution in the region of the highest neutron rate indicating development of significant energetic tails above 25 keV. **(C)** Temporal evolution of the *dd* fusion neutron yield rate shows the majority of neutron generation within 4 ps of main pulse arrival. By assuming cylindrical symmetry around the laser axis, we estimate a total neutron yield of 4×10^9.

5 Conclusion

Combining a thin, several micron-scale cryogenic deuterium target with a petawatt-class laser, we obtained a total deuteron yield of 10^{13}/shot with efficient ~ 8 – 10% energy transfer from the laser. This high deuteron yield supported a high neutron yield $\gtrsim 10^{10}$ and efficiency of 10^8 neutrons/J, comparable to previously published highest neutron yields from laser-driven sources. With 10^{10} neutrons produced by the forward-directed beam in the beryllium catcher, fluences $> 10^9$/cm^2 would have been achieved, primarily in the beam direction in the catcher. Accounting for the nanosecond delay between faster and slower deuterons in the beam, we infer that fluxes exceeding 10^{18}/cm^2/s were obtained at the catcher. If the catcher could be placed closer to the ion source, millimeters away instead of centimeters, this flux could be enhanced by at least an order of magnitude, if not more. Deuteron break-up on Be and Al experimental apparatus explains a majority but not all the observed neutron yield. Identifying the remaining neutrons as derived from *d* (*d*,*n*)^{3}He fusion reactions in the laser-irradiated deuterium jet, we infer a fusion neutron yield (10^7 n/J) and high peak flux ($> 10^{22}$ n/cm^2/s) near the plasma. As a consequence of the much higher neutron contribution from break-up, a signal of fusion was not clearly identifiable in the neutron spectrum. The double peak feature in two observed neutron spectra is currently not fully understood. In future experiments, multiple neutron time-of-flight detectors should be employed to allow coincidence-based background rejection to determine if the second, higher energy peak is due to a physical neutron signal or not. In case this peak represents a real signal, a multiple detector setup also enables extraction of additional information about the location of the source of the signal.

The neutron flux inferred to originate from in-target fusion is almost a million times higher than the laser-ion driven method (10^{17} n/cm^2/s) [26] as well as conventional neutron source like spallation sources (10^{17} n/cm^2/s) and fission reactors (10^{15} n/cm^2/s) [6]. Additional experiments with improved diagnostics (multiple TOF spectrometers and yield measurements out of plane) are necessary to confirm both the yield and *d* (*d*,*n*)^{3}He nature of the source. We anticipate that a thicker target could suppress high energy deuteron emission without significantly reducing the neutron yield. If harnessed and controlled in the right setup, this high peak flux can enable experiments up to now infeasible, for example, the study of the nuclear cross sections and excitation dynamics essential to the r-process [49], responsible for the creation of heavy elements. The key requirement for this research is an extremely high flux of neutrons to allow successive neutron absorption at a rate faster than the decay time. A laser-driven neutron source such as described here introduces additional technical challenges to designing a multi-neutron capture experiment, not least because of the high energy particle and radiation background from the nearby laser-plasma interaction. Future work can stabilize this mechanism as a neutron source and improve the design to begin addressing these challenges. A future multi-beam facility could irradiate a target of interest using two or more laser-driven fusion neutron sources with ultrahigh neutron flux in precision intervals down to ps. This method has potential to significantly increase the peak neutron flux with the next-generation lasers such as 10 PW Extreme Light Infrastructure [50] and multi-PW Apollon laser [51].

Data availability statement

The raw data supporting the conclusions of this article will be made available by the authors, without undue reservation.

Author contributions

XJ led and conducted the experiment and prepared the manuscript. CC, MG, JK, EM, EG, GD, BO-O, CS, RR, GT, GG, FT, and SG prepared the target and helped with the experiment. HC and FF conducted PIC simulations. LL, XJ,

MG. DP, and EM analyzed data. OL contributed to the theory analysis and the manuscript preparation. BH organized the collaboration and contributed to the manuscript contribution.

Funding

Work performed under the auspices of the University of Texas at Austin. This work was supported by the Air Force Office of Scientific Research (FA9550-14-1-0045). High performance computing resources were provided by the Texas Advanced Computing Center and OSIRIS simulations were performed on Cori (NERSC) through ERCAP and ALCC compuational grants. This work used the Extreme Science and Engineering Discovery Environment (XSEDE), which is supported by National Science Foundation grant number ACI-1548562. Development of the cryogenic deuterium jet was supported by the U.S. DOE Office of Science, Fusion Energy Sciences under FWP No. 100182. GG acknowledges support from the U.S. DOE NNSA SSGF program under DE-NA0003960. This material is based upon work supported in part by the National Science Foundation under Grant No. 1632708.

Acknowledgments

We would like to thank the Texas Petawatt laser facility staff for their brilliant and unwavering support.

Conflict of interest

The authors declare that the research was conducted in the absence of any commercial or financial relationships that could be construed as a potential conflict of interest.

Publisher's note

References

1. Wallerstein G, Iben I, Parker P, Boesgaard AM, Hale GM, Champagne AE, et al. Synthesis of the elements in stars: Forty years of progress. *Rev Mod Phys* (1997) 69: 995–1084. doi:10.1103/revmodphys.69.995

2. Yuan V, Bowman JD, Funk D, Morgan G, Rabie R, Ragan C, et al. Shock temperature measurement using neutron resonance spectroscopy. *Phys Rev Lett* (2005) 94:125504. doi:10.1103/physrevlett.94.125504

3. Higginson D, McNaney J, Swift D, Bartal T, Hey D, Kodama R, et al. Laser generated neutron source for neutron resonance spectroscopy. *Phys Plasmas* (2010) 17:100701. doi:10.1063/1.3484218

4. Barth RF, Coderre JA, Vicente MGH, Blue TE. Boron neutron capture therapy of cancer: Current status and future prospects. *Clin Cancer Res* (2005) 11: 3987–4002. doi:10.1158/1078-0432.ccr-05-0035

5. Hill P, Wu Y. Exploring laser-driven neutron sources for neutron capture cascades and the production of neutron-rich isotopes. *Phys Rev C* (2021) 103: 014602. doi:10.1103/physrevc.103.014602

6. Taylor A, Dunne M, Bennington S, Ansell S, Gardner I, Norreys P, et al. A route to the brightest possible neutron source? *Science* (2007) 315:1092–5. doi:10.1126/science.1127185

7. Glenzer S, MacGowan B, Michel P, Meezan N, Suter L, Dixit S, et al. Symmetric inertial confinement fusion implosions at ultra-high laser energies. *Science* (2010) 327:1228–31. doi:10.1126/science.1185634

8. Le Pape S, Berzak Hopkins LF, Divol L, Pak A, Dewald EL, Bhandarkar S, et al. Fusion energy output greater than the kinetic energy of an imploding shell at the national ignition facility. *Phys Rev Lett* (2018) 120:245003. doi:10.1103/physrevlett.120.245003

9. Boehly T, Brown D, Craxton R, Keck R, Knauer J, Kelly J, et al. Initial performance results of the OMEGA laser system. *Opt Commun* (1997) 133: 495–506. doi:10.1016/s0030-4018(96)00325-2

10. Spaeth ML, Manes K, Kalantar D, Miller P, Heebner J, Bliss E, et al. Description of the NIF laser. *Fusion Sci Technol* (2016) 69:25–145. doi:10.13182/fst15-144

11. Mourou DG, Mourou G. Compression of amplified chirped optical pulses. *Opt Commun* (1985) 55:447–9. doi:10.1016/0030-4018(85)90151-8

12. Norreys P, Fews A, Beg F, Bell A, Dangor A, Lee P, et al. Neutron production from picosecond laser irradiation of deuterated targets at intensities of. *Plasma Phys Control Fusion* (1998) 40:175–82. doi:10.1088/0741-3335/40/2/001

13. Zweiback J, Smith R, Cowan T, Hays G, Wharton K, Yanovsky V, et al. Nuclear fusion driven by coulomb explosions of large deuterium clusters. *Phys Rev Lett* (2000) 84:2634–7. doi:10.1103/physrevlett.84.2634

14. Karsch S, Düsterer S, Schwoerer H, Ewald F, Habs D, Hegelich M, et al. *Phys Rev Lett* (2003) 91:015001. doi:10.1103/physrevlett.91.015001

15. Buersgens F, Madison K, Symes D, Hartke R, Osterhoff J, Grigsby W, et al. *Phys Rev E* (2006) 74:016403. doi:10.1103/physreve.74.016403

16. Willingale L, Petrov G, Maksimchuk A, Davis J, Freeman R, Joglekar A, et al. Comparison of bulk and pitcher-catcher targets for laser-driven neutron production. *Phys Plasmas* (2011) 18:083106. doi:10.1063/1.3624769

17. Bang W, Barbui M, Bonasera A, Dyer G, Quevedo H, Hagel K, et al. Temperature measurements of fusion plasmas produced by petawatt-laser-irradiated D_2 – ^{3}He or CD_4 – ^{3}He clustering gases. *Phys Rev Lett* (2013) 111: 055002. doi:10.1103/PhysRevLett.111.055002

18. Jung D, Falk K, Guler N, Deppert O, Devlin M, Favalli A, et al. Characterization of a novel, short pulse laser-driven neutron source. *Phys Plasmas* (2013) 20:056706. doi:10.1063/1.4804640

19. Roth M, Jung D, Falk K, Guler N, Deppert O, Devlin M, et al. *Phys Rev Lett* (2013) 110:044802. doi:10.1103/physrevlett.110.044802

20. Storm M, Jiang S, Wertepny D, Orban C, Morrison J, Willis C, et al. Fast neutron production from lithium converters and laser driven protons. *Phys Plasmas* (2013) 20:053106. doi:10.1063/1.4803648

21. Pomerantz I, McCary E, Meadows AR, Arefiev A, Bernstein AC, Chester C, et al. Ultrashort pulsed neutron source. *Phys Rev Lett* (2014) 113:184801. doi:10.1103/physrevlett.113.184801

22. Hah J, Petrov G, Nees J, He Z-H, Hammig M, Krushelnick K, et al. High repetition-rate neutron generation by several-mJ, 35 fs pulses interacting with free-flowing D2O. *Appl Phys Lett* (2016) 109:144102. doi:10.1063/1.4963819

23. Kar S, Green A, Ahmed H, Alejo A, Robinson A, Cerchez M, et al. Beamed neutron emission driven by laser accelerated light ions. *New J Phys* (2016) 18: 053002. doi:10.1088/1367-2630/18/5/053002

24. Jiao X, Shaw J, Wang T, Wang X, Tsai H, Poth P, et al. A tabletop, ultrashort pulse photoneutron source driven by electrons from laser wakefield acceleration. *Matter Radiat Extremes* (2017) 2:296–302. doi:10.1016/j.mre.2017.10.003

25. Higginson D, McNaney J, Swift D, Petrov G, Davis J, Frenje J, et al. Production of neutrons up to 18 MeV in high-intensity, short-pulse laser matter interactions. *Phys Plasmas* (2011) 18:100703. doi:10.1063/1.3654040

26. Guler N, Volegov P, Favalli A, Merrill FE, Falk K, Jung D, et al. Neutron imaging with the short-pulse laser driven neutron source at the Trident laser facility. *J Appl Phys* (2016) 120:154901. doi:10.1063/1.4964248

27. Gauthier M, Curry C, Göde S, Brack F-E, Kim J, MacDonald M, et al. High repetition rate, multi-MeV proton source from cryogenic hydrogen jets. *Appl Phys Lett* (2017) 111:114102. doi:10.1063/1.4990487

28. Gaul EW, Martinez M, Blakeney J, Jochmann A, Ringuette M, Hammond D, et al. Demonstration of a 11 petawatt laser based on a hybrid optical parametric chirped pulse amplification/mixed Nd:glass amplifier. *Appl Opt* (2010) 49:1676. doi:10.1364/ao.49.001676

29. Kim J, Göde S, Glenzer S. Development of a cryogenic hydrogen microjet for high-intensity, high-repetition rate experiments. *Rev Sci Instrum* (2016) 87:11E328. doi:10.1063/1.4961089

30. Curry CB, Schoenwaelder C, Goede S, Kim JB, Rehwald M, Treffert F, et al. Cryogenic liquid jets for high repetition rate Discovery science. *J Visualized Experiments* (2020) 159:e61130. doi:10.3791/61130

31. Obst L, Göde S, Rehwald M, Brack F-E, Branco J, Bock S, et al. *Scientific Rep* (2017) 7:1. doi:10.1038/s41598-017-10589-3

32. Curry C, Dunning C, Gauthier M, Chou H-G, Fiuza F, Glenn G, et al. Optimization of radiochromic film stacks to diagnose high-flux laser-accelerated proton beams. *Rev Scientific Instr* (2020) 91:093303. doi:10.1063/5.0020568

33. Gauthier M, Kim J, Curry C, Aurand B, Gamboa E, Göde S, et al. High-intensity laser-accelerated ion beam produced from cryogenic micro-jet target. *Rev Sci Instrum* (2016) 87:11D827. doi:10.1063/1.4961270

34. Ing H, Noulty R, McLean T. Bubble detectors-A maturing technology. *Radiat measurements* (1997) 27:1–11. doi:10.1016/s1350-4487(96)00156-4

35. Alejo A, Kar S, Ahmed H, Krygier A, Doria D, Clarke R, et al. Characterisation of deuterium spectra from laser driven multi-species sources by employing differentially filtered image plate detectors in Thomson spectrometers. *Rev Scientific Instr* (2014) 85:093303. doi:10.1063/1.4893780

36. Allison J, Amako K, Apostolakis J, Araujo H, Arce Dubois PA, Asai M, et al. Geant4 developments and applications. *IEEE Trans Nucl Sci* (2006) 53:270–8. doi:10.1109/tns.2006.869826

37. Abramovich S, Generalov L, Zvenigorodskij A. Izvestiya akademii nauk. Rossijskaya akademiya nauk. *Seriya Fizicheskaya* (1999) 63:76.

38. Bém P, Šimečková E, Honusek M, Fischer U, Simakov S, Forrest R, et al. Low and medium energy deuteron-induced reactions on Al27. *Phys Rev C* (2009) 79:044610. doi:10.1103/physrevc.79.044610

39. Ménard S, Mirea M, Clapier F, Pauwels N, Proust J, Donzaud C, et al. Fast neutron forward distributions from C, Be, and U thick targets bombarded by deuterons. *Phys Rev Spec Topics-Accelerators Beams* (1999) 2:033501. doi:10.1103/physrevstab.2.033501

40. Pampus J, Bisplinghoff J, Ernst J, Mayer-Kuckuk T, Rama Rao JR, Baur G, et al. Inclusive proton spectra from deuteron break-up: Theory and experiment. *Nucl Phys A* (1978) 311:141–60. doi:10.1016/0375-9474(78)90506-7

41. Matsuoka N, Kondo M, Shimizu A, Saito T, Nagamachi S, Sakaguchi H, et al. Deuteron break-up in the fields of nuclei at 56 MeV. *Nucl Phys A* (1980) 345:1–12. doi:10.1016/0375-9474(80)90409-1

42. Chittenden BJ, Chittenden J. The production spectrum in fusion plasmas. *Plasma Phys Control Fusion* (2011) 53:045002. doi:10.1088/0741-3335/53/4/045002

43. Brenner CM, Robinson A, Markey K, Scott R, Gray R, Rosinski M, et al. High energy conversion efficiency in laser-proton acceleration by controlling laser-energy deposition onto thin foil targets. *Appl Phys Lett* (2014) 104:081123. doi:10.1063/1.4865812

44. Fonseca RA, Silva LO, Tsung FS, Decyk VK, Lu W, Ren C, et al. Osiris: A three-dimensional, fully relativistic particle in cell code for modeling plasma based accelerators. In: PMA Sloot, AG Hoekstra, CJK Tan, JJ Dongarra, editors. *Computational science — ICCS 2002: International conference amsterdam, The Netherlands, april 21–24, 2002 proceedings, Part III*. Berlin, Heidelberg: Springer Berlin Heidelberg (2002). p. 342–51. doi:10.1007/3-540-47789-6_36

45. Fonseca RA, Martins SF, Silva LO, Tonge JW, Tsung FS, Mori WB. One-to-one direct modeling of experiments and astrophysical scenarios: Pushing the envelope on kinetic plasma simulations. *Plasma Phys Controlled Fusion* (2008) 50:9. doi:10.1088/0741-3335/50/12/124034

46. Yin L, Albright B, Bowers K, Jung D, Fernández J, Hegelich B. Three-dimensional dynamics of breakout afterburner ion acceleration using high-contrast short-pulse laser and nanoscale targets. *Phys Rev Lett* (2011) 107:045003. doi:10.1103/physrevlett.107.045003

47. Mishra R, Fiuza F, Glenzer S. Enhanced ion acceleration in transition from opaque to transparent plasmas. *New J Phys* (2018) 20:043047. doi:10.1088/1367-2630/aab8db

48. Bosch HS, Hale GM. Improved formulas for fusion cross-sections and thermal reactivities. *Nucl Fusion* (1992) 32:611–31. doi:10.1088/0029-5515/32/4/i07

49. Bartlett A, Görres J, Mathews GJ, Otsuki K, Wiescher M, Frekers D, et al. Two-neutron capture reactions and the *r* process. *Phys Rev C* (2006) 74:015802. doi:10.1103/physrevc.74.015802

50. Gales S, Tanaka K, Balabanski D, Negoita F, Stutman D, Tesileanu O, et al. The extreme light infrastructure-nuclear physics (ELI-NP) facility: New horizons in physics with 10 PW ultra-intense lasers and 20 MeV brilliant gamma beams. *Rep Prog Phys* (2018) 81:094301. doi:10.1088/1361-6633/aacfe8

51. Papadopoulos D, Zou J, Le Blanc C, Chériaux G, Georges P, Druon F, et al. The Apollon 10 PW laser: Experimental and theoretical investigation of the temporal characteristics. *High Power Laser Sci Eng* (2016) 4:e34. doi:10.1017/hpl.2016.34

Appendix A: Laser temporal profile

The Texas Petawatt laser temporal profile is measured without a plasma mirror. Figure 6 shows a coarse scan (blue) revealing a long prepulse extending > 20 ps before the peak. The fine scan (orange) around the peak determines the intensity FWHM pulse duration of 135 fs. A plasma mirror enhances the contrast by approximately the ratio between the mirror reflectivity before being triggering and the mirror reflectivity after triggered. The reflectivity before triggering is determined by the coating's reflectivity averaged over angle of incidence and spectral bandwidth of the laser. This ratio leads to an expected contrast enhancement of ~ 200.

For the expected peak intensity of the laser we estimate that the plasma mirror would trigger about 6 ps before the peak. Therefore, we model (green line) the effect of the plasma mirror by rapidly suppressing the laser field strength 6 ps before the peak, which also provides a well-defined starting point for evolution in the simulation.

Appendix B: RCF formula

From front to back: 13 μm Al + HDv2 + 8×(100 μm Al + HDv2) + 6×(150 μm Cu + MDv3) + 16×(500 μm Cu + EBT3) + 5×(1 mm Cu + EBT3). HDv2 is Mylar, thickness 105 μm, MDv3 is Mylar, thickness: 260 μm, and EBT3 is Mylar, thickness 280 μm.